



Single atom Pd anchored-MnO confined in porous carbon matrix for low-level VOCs removal at room temperature

Yuxuan Li^a, Pengyi Zhang^{a,b,*}, Yan Liu^a

^a State Key Joint Laboratory of Environment Simulation and Pollution Control, School of Environment, Tsinghua University, Beijing 100084, China

^b Beijing Key Laboratory for Indoor Air Quality Evaluation and Control, Beijing 100084, China

ARTICLE INFO

Keywords:

Single-atom
MOF derivative
Low-level VOC
Adsorption
Catalytic oxidation

ABSTRACT

Sustainably removing low-level VOCs at room temperature especially in the presence of water vapor has great demand. Herein, single-atom Pd anchored MnO nanoparticles (Pd/MnO) were confined in the hydrophobic porous carbon matrix. As-synthesized Pd/MnO@C exhibited superior removal capacity for VOCs such as hexanal, pentanal and toluene. Under the WHSV of 450 L/g·h, the 99% removal capacity for 15 ppm hexanal at 30 °C and relative humidity (RH) 50% reached 388.8 mg/g, which was 2.4 times as that of commercial BPL activated carbon. In addition, it exhibited much better regeneration ability at low temperature (105 °C) than activated carbon. *In-situ* DRIFTS and EPR indicated that water vapor mediated the activation of oxygen to form hydroxyl radicals to decompose VOCs. This paper opens a new way to sustainably remove low-level VOCs at room temperature under humid conditions via the hydrophobic carbon confinement effect and single-atom catalysis.

1. Introduction

Volatile organic compounds (VOCs) have significant adverse effects on human health, which are crucial contributors to global morbidity and mortality [1,2]. As one kind of main pollutants, VOCs may be smelly, toxic, mutagenic, and carcinogenic [3,4]. VOCs originate from many industrial processes. The concentration of VOC produced during the industrial process varies greatly, of which the low-level VOC (several to dozens of ppm) exists in coal-fired flue gas, iron ore sintering process, shoemaking, and painting industries etc. [5–8]. In addition, indoor environment usually suffers from low-level VOCs pollution from furniture, decoration and cooking fumes [9–11]. Up to now, various technologies have been explored for low-level VOCs removal, such as adsorption [12–14], thermal catalytic oxidation [10,15,16], photocatalytic degradation [17,18], plasma oxidation [19,20] and photo-thermal catalytic decomposition [21–23]. Among these methods, conventional adsorbents such as activated carbon and zeolites have been widely used to remove VOCs. Various strategies, such as surface modification, pore structure adjustment and surface area increasing, are employed to enlarge adsorption capacity [24–26]. Besides conventional adsorbents, many kinds of metal organic frameworks (MOFs) have been synthesized to remove VOCs [27,28]. However, the adsorption capacity

of adsorbents is a function of adsorbate concentration, which sharply decreases to a very low value when the VOC concentration at the several ppm-level [13,29].

As for catalytic oxidation, it has been realized for formaldehyde (HCHO) to be quickly decomposed into CO₂ by noble metal and MnO₂ at room temperature [30,31]. However, the room-temperature decomposition of VOCs containing multi-carbon have been less investigated, and they are more difficult to be completely decomposed due to their more stable molecular structure. For examples, Xu et al. [30] first reported the room-temperature mineralization of acetic acid by ultrathin δ-MnO₂ nanoribbons under RH 50%, and the 100% removal capacity for 1.23 ppm acetic acid under the weight-hourly space velocity (WHSV) of 600 L/g·h was ~ 20.8 mg/g. Hu et al. [10] recently reported the room-temperature catalytic removal of hexanal under RH 50% by ultrafine α-MnO₂ nanowires (~ 5 nm), and the 100% removal capacity for 4.0 ppm and 1.0 ppm hexanal reached 40 mg/g and 50.4 mg/g, respectively. Zhang et al. [16,32] achieved the room-temperature catalytic removal of trace toluene (0.42–0.50 ppm) by single-atom Pt or rare-earth La doped MnO₂ under dry condition, and the corresponding 100% removal capacity was 5.96 mg/g. In a word, though the room-temperature catalytic oxidation of VOCs such as acetic acid, hexanal and toluene has been realized, the corresponding one-through

* Corresponding author at: State Key Joint Laboratory of Environment Simulation and Pollution Control, School of Environment, Tsinghua University, Beijing 100084, China.

E-mail address: zpy@tsinghua.edu.cn (P. Zhang).

<https://doi.org/10.1016/j.apcatb.2024.124139>

Received 19 February 2024; Received in revised form 14 April 2024; Accepted 27 April 2024

Available online 29 April 2024

0926-3373/© 2024 Elsevier B.V. All rights reserved.

100% removal capacity is still not high enough for the practical application. Moreover, under humid conditions, the competitive adsorption of high-concentration water vapor (up to tens of thousands of ppm) with low-level VOC would seriously deteriorate the catalytic activity, as well as adsorption capacity.

Therefore, it is necessary to develop new strategy to increase the removal capacity for low-level VOCs and inhibit the adverse impact of ubiquitous water vapor. Combining adsorption and catalysis is one of the effective methods to improve VOC removal. Although a few researchers have tried it before [33–35], many problems still need to be solved. First, catalytic components are difficult to be uniformly dispersed in the porous adsorbents especially in their pores, thus it can't efficiently utilize hydrophobic protection of adsorbents to reduce the adverse impact of water vapor. Secondly, the catalytic activity is not high enough, thus concurrent adsorption and catalytic removal can't be achieved at low temperature especially at room temperature [36]. Third, the regeneration temperature is still relatively high.

In this work, Pd was facilely introduced into the pores of a Mn-based MOF material by the double solvent method. After carbonization, in-situ formed MnO nanoparticles with anchoring of single Pd atoms were confined in porous carbon substrate. As-synthesized Pd/MnO@C displayed excellent concurrent adsorption and catalytic activity for low-level VOCs at room temperature under humid conditions, and it can be regenerated at relatively low temperature. The mechanism for the enhanced VOCs removal capacity was also clarified.

2. Experimental

2.1. Chemical reagents and preparation of catalysts

All chemical reagents were commercially purchased and used with received. Methanol and n-hexane were purchased from Shanghai Titan Scientific Co., Ltd. $\text{Mn}(\text{NO}_3)_2 \cdot 4\text{H}_2\text{O}$ was obtained from Meryer (Shanghai) Chemical Technology Co., Ltd. 1,3,5-benzenetricarboxylic acid was obtained from Shanghai Macklin Biochemical Co., Ltd. PdCl_2 was obtained from Energy Chemical. Standard hexanal and toluene gas were purchased from Jinghui Gas Co., Ltd. The BPL activated carbon used for comparison was purchased from Calgon Carbon Company (USA).

MIL-100(Mn) was synthesized according to the literature [37] with a slight modification. Specifically, 0.84 g of 1,3,5-benzenetricarboxylic acid (4 mmol) and 1 g of $\text{Mn}(\text{NO}_3)_2 \cdot 4\text{H}_2\text{O}$ (4 mmol) were dissolved in 20 mL methanol. Then the matrix was transferred into the Teflon-lined stainless-steel autoclave and heated at 125 °C for 2 h. The brown solid product was separated via centrifugation. The final MIL-100(Mn) was washed with ethanol for 3 times and dried at 60 °C in a vacuum oven.

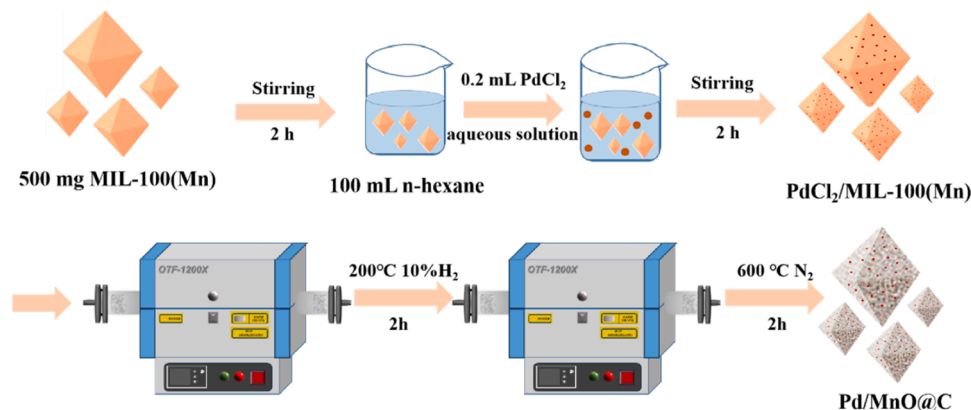
The Pd/MIL-100(Mn) was synthesized using double solvents method, in which water and n-hexane were used as the hydrophilic and

hydrophobic solvent, respectively [38]. First, 500 mg of MIL-100(Mn) was dispersed in a large amount of n-hexane (100 mL), which made the outer surface of MIL-100(Mn) hydrophobic and facilitated the impregnation. After stirring for 2 h, a small amount of aqueous solution of PdCl_2 (0.2 mL) was divided into 4 equal parts and dropped into the above suspension every 5 min. The aqueous solution of PdCl_2 can enter the hydrophilic pores of MIL-100(Mn) through capillary forces, making Pd uniformly dispersed in MIL-100(Mn). The mixture was stirred for another 2 h. Then the PdCl_2 /MIL-100(Mn) composite was carefully separated from n-hexane and dried at 60 °C in the vacuum oven. As-obtained PdCl_2 /MIL-100(Mn) was heated in a tube furnace at 200 °C for 2 h under the flow of 10% H_2 / N_2 . After cooled down to room temperature, the product was further heated at 600 °C for 2 h under the flow of N_2 to yield Pd/MnO@C. Three kinds of MnO@C samples, i.e., MnO@C-500, MnO@C-600, and MnO@C-700 were also obtained by calcining MIL-100(Mn) at corresponding temperatures (500 °C, 600 °C and 700 °C, respectively) without PdCl_2 impregnation. According to the weight ratio of PdCl_2 to MnO@C-600 designed during preparation, three Pd/MnO@C samples were prepared and denoted as Pd-0.25/MnO@C, Pd-0.5/MnO@C and Pd-1.0/MnO@C, respectively.

2.2. Characterization of catalysts

The X-ray diffraction (XRD) patterns were recorded on a Bruker X-ray diffractometer (D8-Advance, Germany) using Cu K α radiation. The morphologies of samples were characterized by Merlin scanning electron microscope (SEM, Carl Zeiss, Germany) and JEM-2011 transmission electron microscope (JEOL, JEM-2100 Japan). High-angle annular dark-field scanning transmission electron microscopy (HAADF-STEM) images were recorded on a Thermo Fisher Scientific Themis Z STEM with probe correctors. X-ray photoelectron spectroscopy (XPS) results were measured on ESCALAB 250Xi X-ray photoelectron spectrometer (Thermo Fisher, USA). The contents of element in the samples were measured with inductively coupled plasma-optical emission spectroscopy (ICP-OES, Thermo IRIS Intrepid II XSP). Electron paramagnetic resonance (EPR) was tested on JEOL FA-200 spectrometer. Pd K-edge XAFS analyses were performed with Si (311) crystal monochromators at the BL14W Beam line at the Shanghai Synchrotron Radiation Facility (SSRF) (Shanghai, China). Data reduction, data analysis, and EXAFS fitting were performed with the Athena and Artemis programs of the Demeter data analysis packages that utilizes the FEFF6 program to fit the EXAFS data. The energy calibration of the sample was conducted through standard Pd foil.

In-situ diffuse reflectance infrared Fourier transform Spectra (DRIFTS) was carried out on a Nicolet 6700 FTIR (Thermo Fisher, USA), which was equipped with an in-situ cell. The sample was first treated at 105 °C for 1 h in the atmosphere of nitrogen. After cooled down to room temperature, hexanal gas (15 ppm, 21 vol% O_2 , N_2 as the balance gas) at



Scheme 1. Procedures for the preparation of MIL-100(Mn) derived Pd/MnO@C.

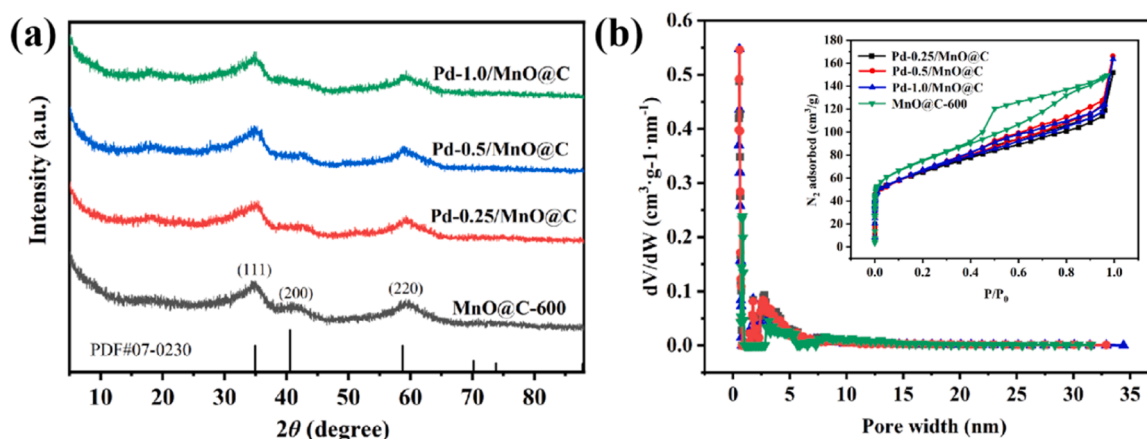


Fig. 1. (a) XRD patterns, (b) N_2 adsorption-desorption isotherms and the pore size distributions of as-synthesized samples.

a flow rate of 50 mL/min was injected and the IR spectra was recorded at certain intervals.

2.3. Evaluation of low-level VOCs removal and decomposition

Breakthrough experiments were conducted to investigate the removal capacity for VOCs at 30 °C and RH 50%. The samples (20 mg, 40–60 mesh) were placed in a fixed-bed quartz tube in a tube furnace, which was used to control the reaction temperature. The flow rates of VOC gas, dry gas and humid gas were adjusted by mass flow controllers. The total gas flow rate was 150 mL/min with the corresponding WHSV of 450 L/g·h. The inlet concentrations of VOCs (hexanal, pentanal and toluene) were detected by GC-2014 (Shimadzu, Japan). The 99% removal capacity was calculated according to Eq. (1).

$$q_e(\text{mg/g}) = \frac{\int_0^t (C_0 - C) \times Q \times dt}{m} \quad (1)$$

where q_e represents VOC 99% removal capacity, i.e., the cumulative removal capacity until the outlet concentration (C) is 1% of inlet concentration (C_0); m is the sample mass; and Q is the volumetric airflow rate.

The hexanal intermediates were tested by thermal desorption (TD-20, Shimadzu, Japan) -mass spectrometry (GCMS-QP 2010 Plus, Shimadzu, Japan). The outlet intermediates and hexanal were first collected with the adsorption tubes filled with 200 mg of Tenax-TA at specific time intervals. Then the adsorption tubes were put onto TD module for further analysis.

3. Results and discussion

3.1. Physicochemical properties of catalysts

The XRD pattern of the as-synthesized MIL-100(Mn) was consistent with that reported in the literature [39] and the simulated single crystal data (Fig. S1), indicating that the pure MIL-100(Mn) was successfully synthesized. After carbonized at 500 °C, 600 °C or 700 °C, weakly crystallized MnO (PDF#07-0230) occurred (Fig. S2) and the crystallinity gradually increased with the carbonization temperature. After loaded with Pd, there were no new peaks and the MnO diffraction peaks showed no significant change (Fig. 1a), indicating that Pd-loading had no obvious effect on the crystallinity of MnO nanoparticles. The weight percentages of Pd in Pd-0.25/MnO@C, Pd-0.5/MnO@C and Pd-1.0/MnO@C measured by ICP-OES were 0.18%, 0.33% and 0.55%, respectively, which indicated that almost all Pd ions were successfully incorporated into the catalysts Scheme 1.

The nitrogen adsorption/desorption curves and the pore size

Table 1

ICP, BET surface area, pore volume and XPS results of different samples.

Sample	Pd (wt %)	BET (m ² /g)	Pore volume (cm ³ /g)	XPS	
				O _{ads} /O _{latt}	Defect carbon (%)
MIL-100(Mn)	-	1726.9	0.802	-	-
MnO@C-500	-	281.3	0.317	1.55	23.18
MnO@C-600	-	263.4	0.217	1.50	30.22
MnO@C-700	-	228.7	0.165	1.50	29.22
Pd-0.25/MnO@C	0.18	230.5	0.194	1.78	22.17
Pd-0.5/MnO@C	0.33	233.0	0.208	2.95	30.25
Pd-1.0/MnO@C	0.55	232.8	0.202	1.59	25.27

distribution of as-synthesized samples are shown in Fig. 1(b), Fig. S3 and S4. And the BET specific surface areas are accordingly calculated (Table 1). The pristine MIL-100(Mn) showed characteristic microporous curves and owned the surface area of 1726.9 m²/g. While its carbonized products showed micro-mesoporous structure and owned much smaller surface area, decreased respectively to 281.3 m²/g, 263.4 m²/g, 228.7 m²/g with increase of carbonization temperature. The loading of Pd further slightly decreased the specific surface area (Table 1).

SEM, TEM and HRTEM images showed the morphology and structure of MIL-100(Mn), MnO@C-600 and Pd-0.5/MnO@C. As shown in Fig. 2a, the particle size of pristine MIL-100(Mn) ranged from 0.4 μm to 2.4 μm. Although some particles exhibited the regular octahedral structure, most of them were fragmented and irregular. Both MnO@C-600 and Pd-0.5/MnO@C maintained the precursor's morphology. TEM and HRTEM images showed that MnO nanoparticles uniformly embedded in the carbon matrix with the size of ~ 4–5 nm. The clear lattice fringe of 0.22 nm (Figs. 2e and 2h) corresponds to the crystal facet (200) of MnO, confirming the XRD results. The selected area electron diffractograms (SAED) of Pd-0.5/MnO@C also displayed the lattice spacing of 2.57 Å, 2.22 Å and 1.57 Å, which could be attributed to (111), (200) and (220) facets of MnO [40]. It is worth noting that no obvious Pd nanoparticles could be observed in TEM and HRTEM images of Pd-0.5/MnO@C, and HAADF-STEM further verified the single atom distribution of Pd in Pd-0.5/MnO@C. As shown in Fig. 3a, there were many single bright spots on the MnO nanoparticles, indicating that Pd single atoms were anchored on MnO rather than on carbon matrix. EDS mapping also suggested the uniform dispersion of Pd atoms throughout the structure. However, in Pd-1.0/MnO@C some of Pd atoms anchored on MnO aggregated into clusters (Fig. 3b).

The Raman spectra of the synthesized materials are shown in Fig. S5. The characteristic peak at 646 cm⁻¹ was assigned to Mn-O vibrational

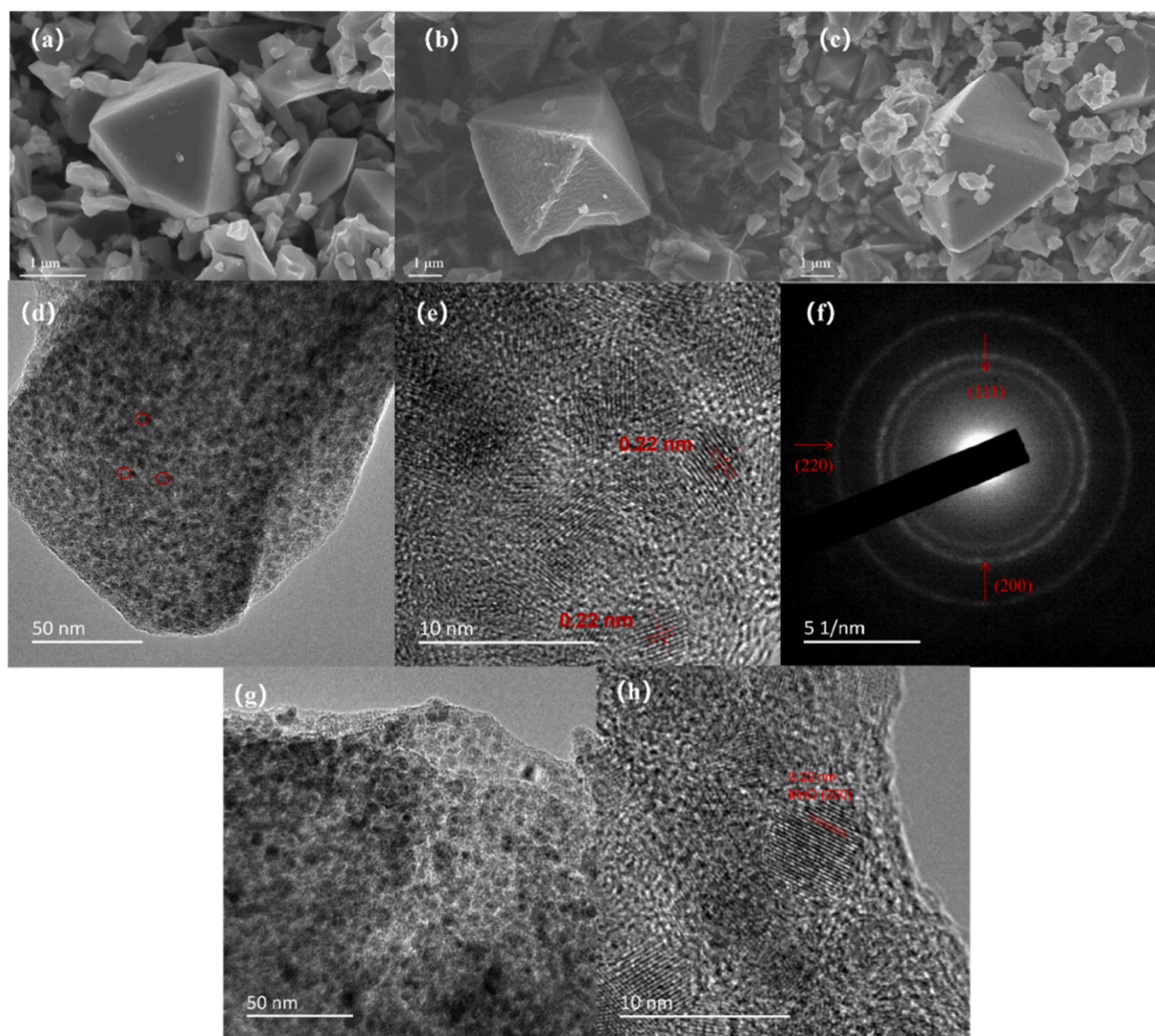


Fig. 2. SEM images of (a) MIL-100(Mn), (b) MnO@C-600 and (c) Pd-0.5/MnO@C. TEM, SAED and HRTEM images of (d, e, f) MnO@C-600 and (g, h) Pd-0.5/MnO@C.

bands, demonstrating the existence of MnO [41]. The typical D band at 1352 cm^{-1} represented the presence of disorder carbon or defective graphite, while the typical G band at 1589 cm^{-1} represented the graphitic structures [42]. The intensity ratio of D band to G band (I_D/I_G) was the highest in the spectra of Pd-0.5/MnO@C, indicating it owned the highest defective carbon [43,44].

The surface chemical composition and valence state were investigated by XPS. The C 1s spectra (Fig. 4a) exhibit the characteristic peaks at 288.5–289.0 eV, 285.6–286.4 eV, 285.3 eV, 284.8 eV and 284.4 eV, which can be attributed to C=O, C-O, defective C-C, C-C and C=C, respectively [43,45–47]. As shown in Table 1, Pd-0.5/MnO@C possessed the highest defective carbon. Combined with Raman analysis, there might be more electron transfer among MnO nanoparticles and surrounding carbon matrix in Pd-0.5/MnO@C, which is beneficial to VOCs oxidation. In Mn 2p spectra (Fig. 4b), the peaks at 641.4 eV, 643.1 eV and 653.4 eV were ascribed to Mn $2p_{3/2}$, satellite peak and Mn $2p_{1/2}$, respectively [48]. The difference of binding energy between Mn $2p_{3/2}$ and Mn $2p_{1/2}$ was 12.0 eV, confirming the existence of Mn(II) and MnO [49]. In O 1s spectra (Fig. 4c), the peaks at 533.6–533.9 eV, 532.5 eV and 530.1 eV represented surface adsorbed water ($O_{\text{adsH}_2\text{O}}$), surface adsorbed oxygen (O_{ads}) and lattice oxygen (O_{latt}), respectively [30,50]. The $O_{\text{ads}}/O_{\text{latt}}$ ratio followed the order: Pd-0.5/MnO@C (2.95) > Pd-0.25/MnO@C (1.78) > Pd-1.0/MnO@C (1.59) > MnO@C-600

(1.50), indicating Pd loading increased the abundance of surface oxygen species and may promote the catalytic performances. The XPS result of Pd 3d (Fig. 4d) showed that there were no significant Pd signal in the spectra of Pd-0.25/MnO@C and Pd-0.5/MnO@C, which could be attributed to the small content of Pd and its existence in the form of single atoms. While Pd-1.0/MnO@C showed two recognizable peaks at 335.7 eV and 340.6 eV corresponding to Pd $3d_{5/2}$ and Pd $3d_{3/2}$ [51], respectively.

To further determine the existence form of Pd in catalysts, the chemical states and coordination environment of Pd atoms were analyzed by using XANES and EXAFS. As shown in Fig. 5a, the XANES result of Pd K-edge showed that the Pd valence state in three catalysts was between Pd foil and PdO, and Pd-0.25/MnO@C owned the highest valence state of Pd, followed by Pd-0.5/MnO@C and Pd-1.0/MnO@C. In the FT-EXAFS (R space) spectra (Fig. 5b), there was obvious peak at $\sim 1.5\text{ \AA}$ attributed to the Pd-O coordination in both Pd-0.25/MnO@C and Pd-0.5/MnO@C, further verifying that Pd exists in the form of single atoms [52]. However, the peak at 2.5 \AA attributed to Pd-Pd became obvious in Pd-1.0/MnO@C, demonstrating the appearance of Pd clusters with increase of Pd content [53].

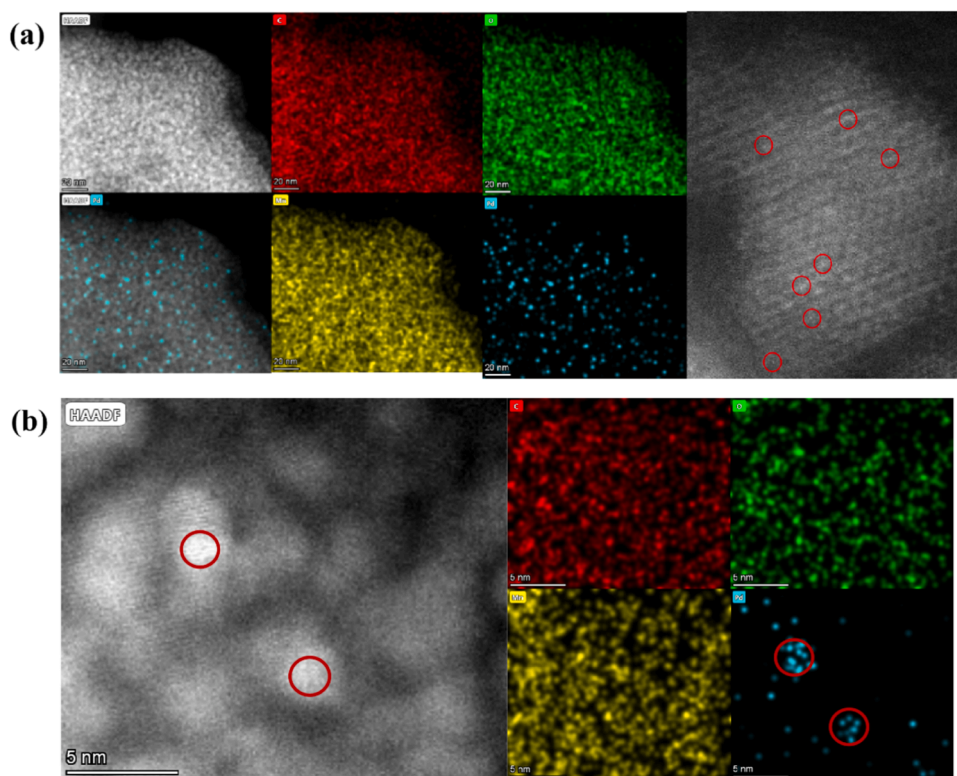


Fig. 3. High-angle annular dark-field STEM images and STEM-EDS images with element distribution images of (a) Pd-0.5/MnO@C, (b) Pd-1.0/MnO@C.

3.2. VOCs removal performance

The hexanal removal performances of as-synthesized catalysts were tested at 30 °C and RH 50% under the WHSV of 450 L/g·h. As shown in Fig. 6a, three types of MnO@C catalysts without Pd loading showed inferior removal performance. Nevertheless, among them, MnO@C-600 demonstrated largest removal capacity for 15 ppm hexanal. Considering that MIL-100(Mn) could not be carbonized completely at 500 °C (Fig. S6) and MnO particles aggregate more easily at higher temperatures, the samples with Pd loading were carbonized at 600 °C. The Pd loading greatly increased the removal capacity for 15 ppm hexanal. Among them, Pd-0.5/MnO@C showed the best performance, its 99% removal capacity for 15 ppm hexanal reached 388.8 mg/g, followed by Pd-1.0/MnO@C (324 mg/g) and Pd-0.25/MnO@C (241.2 mg/g). The above results demonstrated that there are less active sites in Pd-0.25/MnO@C and Pd clusters in Pd-1.0/MnO@C reduced the active sites [54]. For comparison, the adsorption performance of commercial activated carbon for hexanal were also tested under the same conditions. As shown in Fig. 6b, the 99% removal capacity of BPL activated carbon and the wood activated carbon for 15 ppm hexanal was 162 mg/g and 97.2 mg/g, respectively, which was much lower than that of Pd-0.5/MnO@C.

Because Pd-0.5/MnO@C had relatively high specific surface area (233.0 m²/g), the hexanal removal may be partly contributed by physical adsorption. Thus, it is an interesting issue to determine the contribution of adsorption. Here we first deactivated the Pd-0.5/MnO@C at 600 °C in N₂ atmosphere to remove reactive oxygen species and adsorbed water molecules, and then its removal capacity was tested under the N₂ flow. As demonstrated in Fig. 6c, the adsorption capacity for 15 ppm hexanal was ~ 90 mg/g, indicating that adsorption accounted for ~ 23.1% of the hexanal removal and the rest (~76.9%) should be contributed by room-temperature catalysis.

The performance of Pd-0.5/MnO@C under other humidity at 30 °C was also investigated (Fig. S7). The 99% removal capacity for 15 ppm hexanal under dry condition was 172.8 mg/g, and it continuously

increased to 298.8 mg/g under RH 20% and to 388.8 mg/g under RH 50%, respectively. While it decreased to 104.4 mg/g under RH 80% due to the competitive adsorption of water vapor on the active sites and its condensation in pores of carbon matrix.

The regeneration performance of Pd-0.5/MnO@C was also evaluated. After the hexanal removal experiment at 30 °C and RH 50%, Pd-0.5/MnO@C was regenerated at 105 °C in dry air for 4 h. As shown in Fig. 6d, after 3 cycles, the removal capacity of Pd-0.5/MnO@C slightly decreased from 388.8 mg/g to 334.8 mg/g. This phenomenon can be attributed to the incomplete desorption of hexanal and intermediates, which occupied the catalytic active sites. For comparison, the performance of BPL activated carbon was also tested under the same conditions. Its removal capacity significantly decreased from 162.0 mg/g to 61.2 mg/g after 3 cycles, only keeping 38.8% of the initial capacity. The better regeneration performance of Pd-0.5/MnO@C could be ascribed to two reasons. First, MOF-derived porous carbon has interconnected pores, while the porosity connectivity of activated carbon is poor, so MOF-derived carbon can be more easily regenerated at low temperature [55,56]. Secondly, Pd-0.5/MnO@C had low temperature catalytic activity, which increased with the rising of temperature, the adsorbed hexanal and intermediates could be decomposed at 105 °C besides desorption.

Furthermore, the removal capacity of Pd-0.5/MnO@C for other VOCs was also evaluated under the same conditions (30 °C and RH 50%). As shown in Fig. 7a, the 99% removal capacity for 15 ppm pentanal and 10 ppm toluene were 360 mg/g and 137.6 mg/g, respectively. Because the removal capacity may greatly depend on the inlet VOCs concentration, the removal capacity for lower concentration VOCs were also tested. As shown in Fig. 7b, Pd-0.5/MnO@C exhibited much longer breakthrough time for lower concentration VOCs, with 99% removal capacity of 225 mg/g, 182 mg/g and 60 mg/g for 3 ppm hexanal, 3 ppm pentanal and 2 ppm toluene respectively. Though there have been many researches on the removal of low-concentration VOC by adsorption and catalysis, the reported removal performances are not satisfactory. For example, CAU-3(gel) displayed removal capacity of 26.3 mg/g for

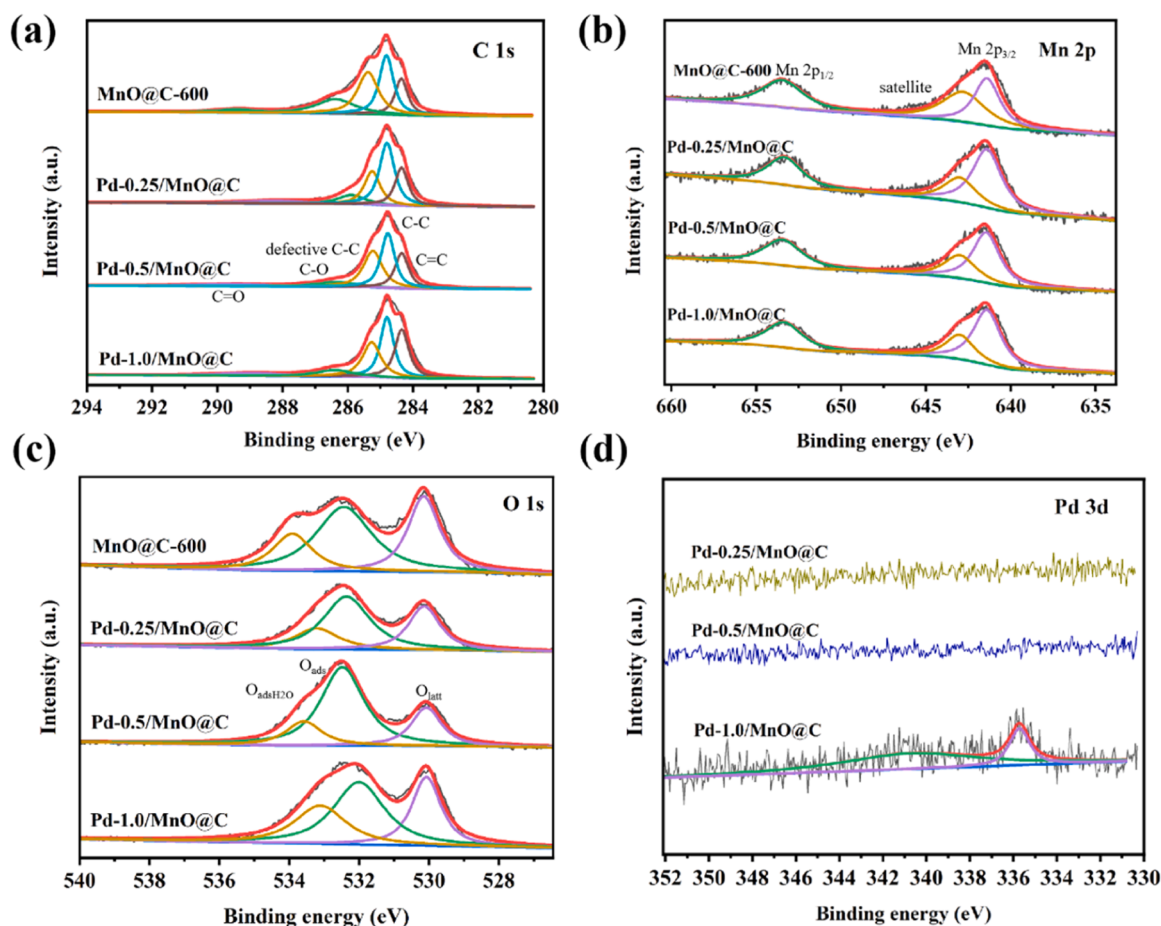


Fig. 4. XPS spectra of as-synthesized materials. (a) C 1 s, (b) Mn 2p, (c) O 1 s, (d) Pd 3d.

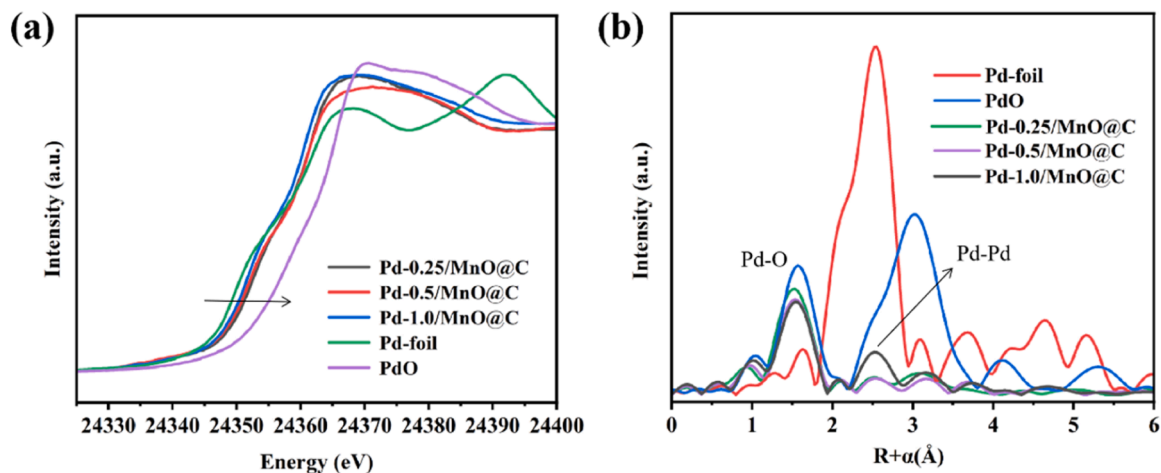


Fig. 5. (a) The normalized XANES spectra at the Pd k edge of Pd foil, PdO and Pd/MnO@C; (b) FT-EXAFS of Pd-0.25/MnO@C, Pd-0.5/MnO@C and Pd-1.0/MnO@C.

2 ppm hexanal at RH 50% under the WHSV of 600 L/g·h [57]. La/MnO₂ exhibited removal capacity of only 5.96 mg/g for 0.5 ppm of toluene at RH 0% under the WHSV of 300 L/g·h [16]. Compared with related materials in literatures (Table S1), as-synthesized Pd-0.5/MnO@C showed the highest capacity for low-level VOCs at room temperature under humid conditions, demonstrating that concurrent room-temperature adsorption and catalysis is an effective strategy to improve the removal capacity for low-level VOCs.

3.3. Catalytic mechanism and hexanal decomposition pathways

To further learn the hydrophobicity of Pd-0.5/MnO@C and its room temperature catalytic mechanism, the *in-situ* DRIFTS at 30 °C under various conditions were investigated. The sample was first pretreated at 105 °C for 1 h in N₂ before test to remove any residuals. As shown in Fig. 8a, when water vapor passed through Pd-0.5/MnO@C catalyst, only weak peaks occurred at 3410 cm⁻¹ and 1630 cm⁻¹ accounting for H₂O

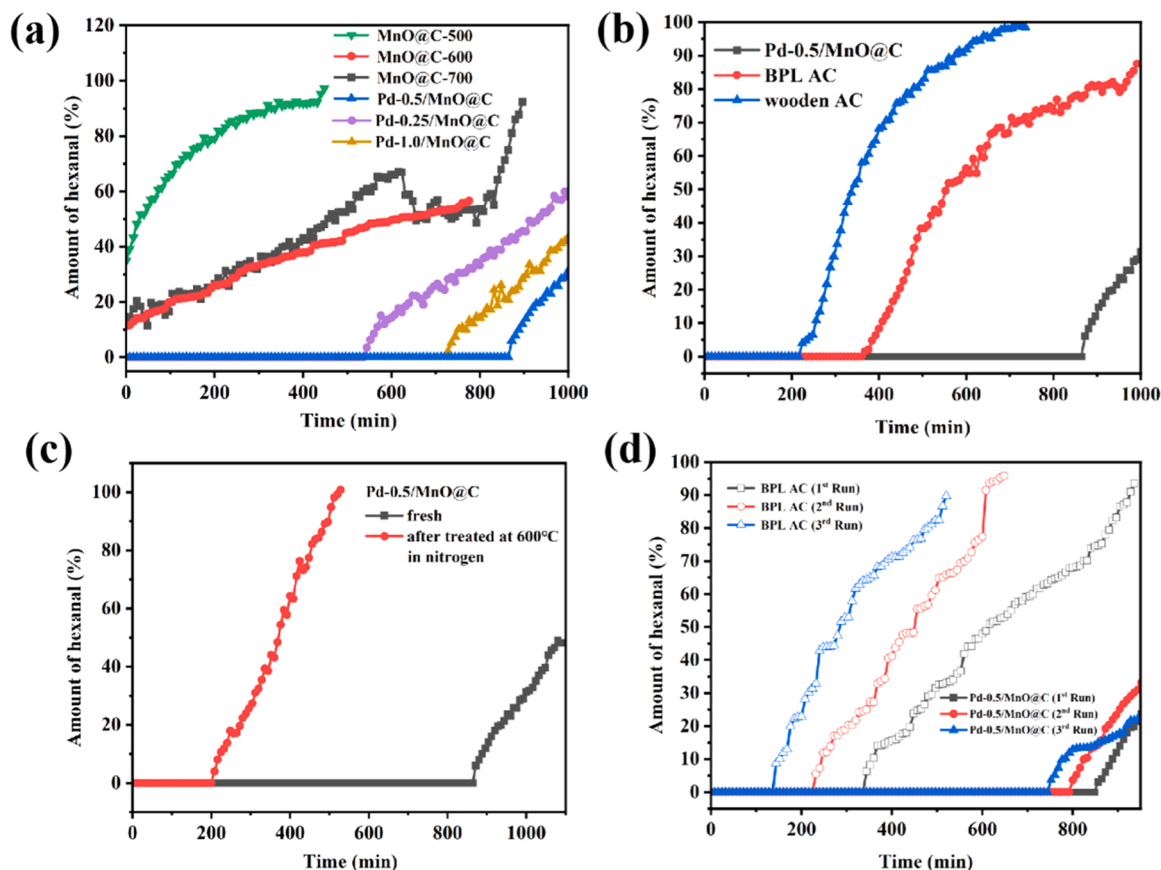


Fig. 6. Breakthrough curves of different materials for 15 ppm hexanal at 30 °C and RH 50% under the WHSV of 450 L/g·h. (a) As-synthesized Mn-based materials; (b) Pd-0.5/MnO@C and two types of activated carbon; (c) Pd-0.5/MnO@C after treated at 600 °C in nitrogen; (d) Pd-0.5/MnO@C and BPL activated carbon regenerated at 105 °C in air.

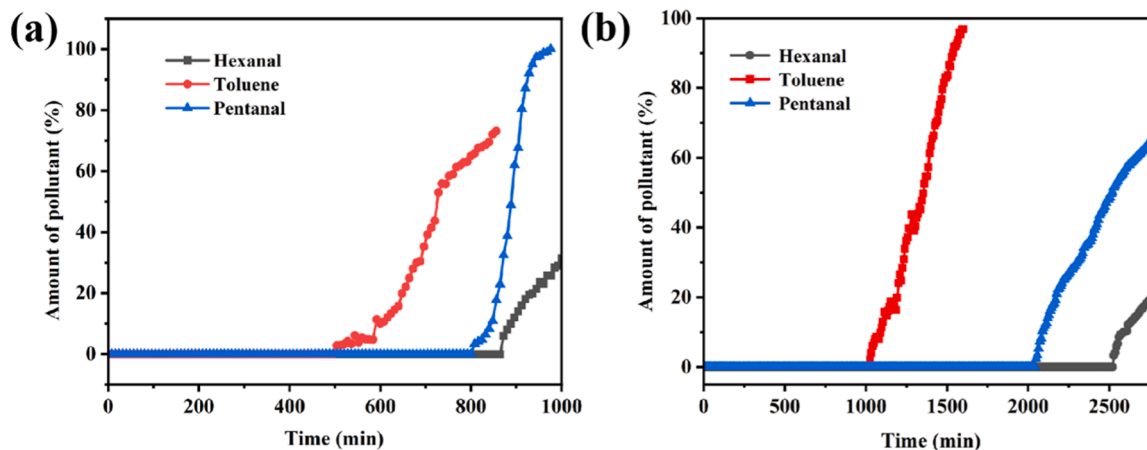


Fig. 7. Breakthrough curves of as-synthesized Pd-0.5/MnO@C for hexanal, toluene and pentanal at 30 °C and RH 50% under WHSV of 450 L/g·h. (a) inlet concentration: hexanal 15 ppm, pentanal 15 ppm, toluene 10 ppm; (b) Inlet concentration: hexanal 3 ppm, pentanal 3 ppm, toluene 2 ppm.

adsorption [30,58], confirming the hydrophobicity of Pd-0.5/MnO@C. In addition, the negative peak at 2330 cm^{-1} can be attributed to the desorption of surface CO_2 [16], indicating that water vapor purged the surface CO_2 .

Fig. 8b shows the *in situ* DRIFTS of Pd-0.5/MnO@C under the flow of dry air containing hexanal. Strong peaks at 2950 , 2927 , 2861 , 2813 and 2711 cm^{-1} were assigned to $\nu_{\text{CH}_3}^{\text{as}}$, $\nu_{\text{CH}_2}^{\text{as}}$, $\nu_{\text{CH}_3}^{\text{s}}$ and $\nu_{\text{C-H}}$ species, respectively [10,59]. Besides, a very sharp peak at 1719 cm^{-1} can be attributed to the C=O vibration of hexanal [60], indicating the strong

adsorption of hexanal on the surface of Pd-0.5/MnO@C. However, there were no obvious characteristic peaks of any intermediates and CO_2 , indicating in the absence of water vapor no catalytic decomposition occurred at room temperature.

Fig. 8c shows the *in-situ* DRIFTS of Pd-0.5/MnO@C under the flow of humid (RH 50%) hexanal-containing air. In the presence of water vapor, the peaks at 2376 cm^{-1} and 2320 cm^{-1} attributed to CO_2 [61] increased with time, as well as the peaks at 1566 cm^{-1} and 1340 cm^{-1} attributed to the symmetric and asymmetric stretching vibration of carboxylate

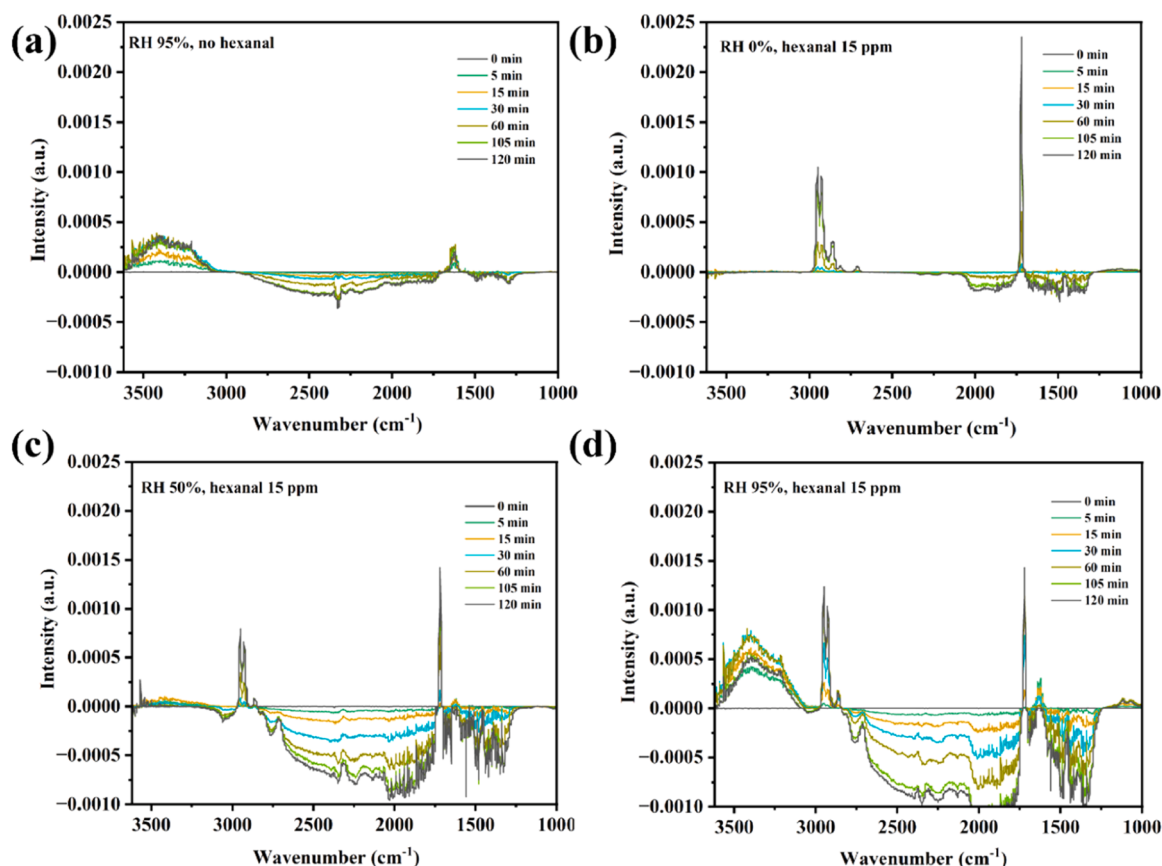


Fig. 8. *In situ* DRIFTS of Pd-0.5/MnO@C at 30 °C under various conditions. (a) RH 100% without hexanal; (b) 15 ppm of hexanal, RH 0%; (c) 15 ppm of hexanal, RH 50%; (d) 15 ppm of hexanal, RH 95%.

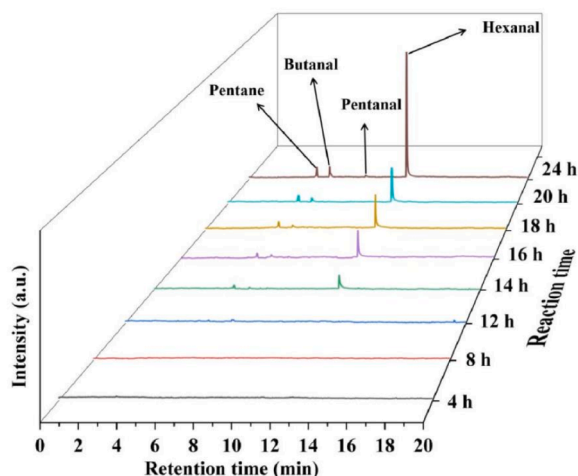


Fig. 9. Time-dependence of outlet hexanal and its intermediates during hexanal decomposition by Pd-0.5/MnO@C (Test conditions: inlet hexanal concentration 15 ppm, 21% O₂/N₂, 30 °C, RH 50%, WHSV 450 L/g·h).

(COO⁻) [10,59]. These results confirmed that in the presence of water vapor hexanal were decomposed over Pd-0.5/MnO@C at room temperature, i.e., water vapor stimulated the catalytic activity of Pd-0.5/MnO@C. The water-mediated activation of O₂ over Au/TiO₂ interface was also reported for CO oxidation [62], where the presence of water can lower the reaction activation barrier by forming OOH groups with adsorbed oxygen. Similarly, we think in this case water vapor also mediates the activation of O₂ over Pd/MnO to form active oxygen

species, and single Pd atoms enhance the activation efficiency. As shown in Fig. S8, EPR analysis clearly showed Pd-0.5/MnO@C had abundant oxygen vacancies, and in the aqueous solution the most OH radicals were generated at room temperature. It is worth noting that even under RH 50% (Fig. 8c), the signals of H₂O adsorption were still very weak, while the hexanal peaks decreased slightly, further confirming the strong hydrophobicity of Pd-0.5/MnO@C catalyst. When the RH further increased to 95%, as shown in Fig. 8d, the peaks of H₂O adsorption became significant. However, the peak at 1630 cm⁻¹ did not proportionally increase with the peak at 3410 cm⁻¹, implying there are at least two different adsorption sites of H₂O on Pd-0.5/MnO@C. In addition, the peaks of adsorbed hexanal were not obviously influenced, while new peaks at 1116 cm⁻¹ and 1070 cm⁻¹ attributed to C-O of carboxyl group increased with time, reflecting the accumulation of hexanal intermediates. Simultaneously, the peak of CO₂ at 2376 cm⁻¹ and 2310 cm⁻¹ slightly became weaker than those in Fig. 8c, indicating even under RH 95% Pd-0.5/MnO@C catalyst can still effectively decompose hexanal.

To learn the decomposition pathway of hexanal at room temperature, TD-GC/MS was used to detect the outlet intermediates. Fig. 9 shows the time dependence of outlet hexanal and its intermediates decomposed by Pd-0.5/MnO@C. There were no significant products detected in the first 8 h. A small amount of pentane and butanal started to be detected at 12 h and increased with time. The breakthrough of hexanal occurred at 14 h, and a very small amount of pentanal was detected at 20 h. The time dependent concentrations of all these intermediates and hexanal are shown in Table S2. Among them, pentane showed the highest concentration, followed by butanal and pentanal, implying hexanal decomposed step by step at room temperature by Pd-0.5/MnO@C, accompanied by the generation of CO₂. No other gaseous intermediates were detected due to the following reasons. One is that

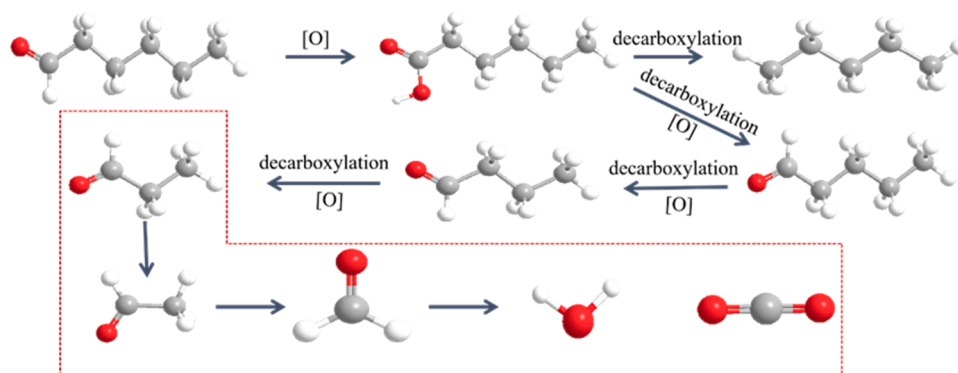


Fig. 10. The step-by-step decomposition pathway of hexanal by Pd-0.5/MnO@C at room temperature.

some products such as carboxylic acids had poor volatility and accumulated on the catalyst surface as illustrated by *in-situ* DRIFTS (Fig. 8c, 8d); and the other one is that some intermediates were rapidly decomposed as soon as they were produced, thus their concentration was too low to be detected in the gas phase.

According to the above analysis results, the step-by-step decomposition pathway of hexanal is proposed (Fig. 10). First, hexanal is oxidized into hexanoic acid, which is soon decarboxylated to generate CO₂, pentanal or pentane. The pentanal is further oxidized into pentanoic acid, which is then decarboxylated into CO₂, butanal or butane. And butanal was further step by step decomposed into CO₂ in the similar mode.

4. Conclusions

A composite catalyst, i.e., Pd single atoms-anchored MnO nanoparticles confined in porous carbon matrix, Pd-MnO@C, was successfully prepared by using Mn-based MOF as precursor and followed by double solvent immersion and carbonization at 600 °C. The hydrophobic porous carbon matrix effectively prevents a large amount of water vapor from occupying the active sites of Pd-anchored MnO nanoparticles, while a small amount of infiltration water molecules mediates the activation of oxygen to form a large amount of active oxygen species such as hydroxyl radicals ($\cdot\text{OH}$), realizing the room temperature decomposition of VOCs including hexanal, pentanal and toluene. As synthesized Pd-0.5/MnO@C exhibited high removal capacity for VOCs under humid conditions, its 99% removal capacity for 15 ppm hexanal at 30 °C and RH 50% was 2.4 times as that of BPL activated carbon. In addition, it could be effectively regenerated at relatively low temperature (105 °C) with better recycling ability than BPL activated carbon. This study provides a new method for the preparation of porous carbon confined metal oxide nanoparticles anchored with precious metal single atoms, and demonstrates a new strategy for sustainably removal of low-level VOCs at room temperature under humid conditions.

CRediT authorship contribution statement

Yan Liu: Formal analysis, Data curation. **Yuxuan Li:** Writing – original draft, Investigation, Data curation. **Pengyi Zhang:** Writing – review & editing, Supervision, Funding acquisition, Conceptualization.

Declaration of Competing Interest

The authors declare that they have no known competing financial interests or personal relationship that could have appeared to influence the work reported in this paper.

Data availability

Data will be made available on request.

Acknowledgments

This work was financially supported by the National Natural Science Foundation of China (No. 22076094), Science & Technology Innovation Program of Shunde of Foshan City (No. 2130218002526) and Tsinghua-Foshan Innovation Special Fund (No. 2021THFS0503).

Appendix A. Supporting information

Supplementary data associated with this article can be found in the online version at doi:10.1016/j.apcatb.2024.124139.

References

- [1] J. González-Martín, N.J.R. Kraakman, C. Pérez, R. Lebrero, R. Muñoz, A state-of-the-art review on indoor air pollution and strategies for indoor air pollution control, *Chemosphere* 262 (2021) 128376.
- [2] D.Y.C. Leung, Outdoor-indoor air pollution in urban environment: challenges and opportunity, *Front. Environ. Sci.* (2) (2015).
- [3] X. Zhang, B. Gao, A.E. Creamer, C. Cao, Y. Li, Adsorption of VOCs onto engineered carbon materials: a review, *J. Hazard. Mater.* 338 (2017) 102–123.
- [4] Y. Guo, M. Wen, G. Li, T. An, Recent advances in VOC elimination by catalytic oxidation technology onto various nanoparticles catalysts: a critical review, *Appl. Catal. B: Environ.* 281 (2021) 119447.
- [5] J. Li, X. Ma, H. Wu, L. Yang, Adsorption of low-concentration VOCs on modified activated carbons in a humid atmosphere, *Energy Fuels* 35 (2021) 5090–5100.
- [6] S. Peishi, Y. Xianwan, H. Ruohua, H. Bing, Y. Ping, A new approach to kinetics of purifying waste gases containing volatile organic compounds (VOC) in low concentration by using the biological method, *J. Clean. Prod.* 12 (2004) 95–100.
- [7] Y. Wang, L. Ding, Q. Shi, S. Liu, L. Qian, Z. Yu, H. Wang, J. Lei, Z. Gao, H. Long, C. Charles, Xu, Volatile organic compounds (VOC) emissions control in iron ore sintering process: Recent progress and future development, *Chem. Eng. J.* 448 (2022) 137601.
- [8] M. Wang, J. Xiao, N. Li, Q. Xu, H. Li, D. Chen, J. Lu, Surface engineering of ternary mixed transition metal oxides for highly efficient catalytic oxidation of low concentration VOCs, *Sep. Purif. Technol.* 334 (2024) 126000.
- [9] J. Kong, T. Yang, Z. Rui, H. Ji, Perovskite-based photocatalysts for organic contaminants removal: current status and future perspectives, *Catal. Today* 327 (2019) 47–63.
- [10] T. Hu, S. Sui, J. Li, P. Zhang, Room-temperature catalytic removal of indoor trace hexanal by weakly crystallized MnO₂ ultrafine nanowires, *Build. Environ.* 226 (2022) 109701.
- [11] C.-Y. Peng, C.-H. Lan, P.-C. Lin, Y.-C. Kuo, Effects of cooking method, cooking oil, and food type on aldehyde emissions in cooking oil fumes, *J. Hazard. Mater.* 324 (2017) 160–167.
- [12] L. Zhu, D. Shen, K.H. Luo, A critical review on VOCs adsorption by different porous materials: species, mechanisms and modification methods, *J. Hazard. Mater.* 389 (2020) 122102.
- [13] X. Zheng, S. Liu, S. Rehman, Z. Li, P. Zhang, Highly improved adsorption performance of metal-organic frameworks CAU-1 for trace toluene in humid air via sequential internal and external surface modification, *Chem. Eng. J.* 389 (2020) 123424.
- [14] T. He, X.-J. Kong, Z.-X. Bian, Y.-Z. Zhang, G.-R. Si, L.-H. Xie, X.-Q. Wu, H. Huang, Z. Chang, X.-H. Bu, M.J. Zaworotko, Z.-R. Nie, J.-R. Li, Trace removal of benzene

- vapour using double-walled metal–dipyrazolate frameworks, *Nat. Mater.* 21 (2022) 689–695.
- [15] R. Liu, H. Wu, J. Shi, X. Xu, D. Zhao, Y.H. Ng, M. Zhang, S. Liu, H. Ding, Recent progress on catalysts for catalytic oxidation of volatile organic compounds: a review, *Catal. Sci. Technol.* 12 (2022) 6945–6991.
 - [16] H. Zhang, X. Zheng, T. Xu, P. Zhang, Atomically dispersed Y or La on birnessite-type MnO_2 for the catalytic decomposition of low-concentration toluene at room temperature, *ACS Appl. Mater. Interfaces* 13 (2021) 17532–17542.
 - [17] S. Almaie, V. Vatanpour, M.H. Rasoulifard, I. Koyuncu, Volatile organic compounds (VOCs) removal by photocatalysts: a review, *Chemosphere* 306 (2022) 135655.
 - [18] A. Maciucă, C. Batiot-Dupeyrat, J.-M. Tatibouët, Synergetic effect by coupling photocatalysis with plasma for low VOCs concentration removal from air, *Appl. Catal. B: Environ.* 125 (2012) 432–438.
 - [19] O. Karatam, M.A. Deshusses, A comparative study of dilute VOCs treatment in a non-thermal plasma reactor, *Chem. Eng. J.* 294 (2016) 308–315.
 - [20] X. Zhu, X. Gao, C. Zheng, Z. Wang, M. Ni, X. Tu, Plasma-catalytic removal of a low concentration of acetone in humid conditions, *RSC Adv.* 4 (2014) 37796–37805.
 - [21] P. Wu, X. Jin, Y. Qiu, D. Ye, Recent progress of thermocatalytic and photo/thermocatalytic oxidation for VOCs purification over manganese-based oxide catalysts, *Environ. Sci. Technol.* 55 (2021) 4268–4286.
 - [22] J. Kong, S. Song, W. Zhao, Z. Yu, Z. Xiang, G. Li, W. Zhang, T. An, Unraveling a trade-off between positive effect and poisoning mechanism of soot over low-dose PtCu/CeO₂ for simultaneously photothermocatalytic removal of VOCs and soot, *Appl. Catal. B: Environ.* 339 (2023) 123118.
 - [23] N. Zhang, W. He, Z. Cheng, J. Lu, Y. Zhou, D. Ding, S. Rong, Construction of $\alpha\text{-MnO}_2/\text{g-C}_3\text{N}_4$ Z-scheme heterojunction for photothermal synergistic catalytic decomposition of formaldehyde, *Chem. Eng. J.* 466 (2023) 143160.
 - [24] Z. Li, Y. Jin, T. Chen, F. Tang, J. Cai, J. Ma, Trimethylchlorosilane modified activated carbon for the adsorption of VOCs at high humidity, *Sep. Purif. Technol.* 272 (2021) 118659.
 - [25] S. Wu, Y. Wang, C. Sun, T. Zhao, J. Zhao, Z. Wang, W. Liu, J. Lu, M. Shi, A. Zhao, L. Bu, Z. Wang, M. Yang, Y. Zhi, Novel preparation of binder-free Y/ZSM-5 zeolite composites for VOCs adsorption, *Chem. Eng. J.* 417 (2021) 129172.
 - [26] Y. Zhang, Q. Yu, Y. Yuan, X. Tang, S. Zhao, H. Yi, Adsorption behavior of Mo-MEL zeolites for reducing VOCs from cooking oil fumes, *Sep. Purif. Technol.* 322 (2023) 124059.
 - [27] M.I. Severino, A. Al Mohtar, C. Vieira Soares, C. Freitas, N. Sadovnik, S. Nandi, G. Mouchaham, V. Pimenta, F. Nouar, M. Daturi, G. Maurin, M.L. Pinto, C. Serre, MOFs with open metal(III) sites for the environmental capture of polar volatile organic compounds, *Angew. Chem. Int. Ed.* 62 (2023) e202211583.
 - [28] C.-Y. Huang, M. Song, Z.-Y. Gu, H.-F. Wang, X.-P. Yan, Probing the adsorption characteristic of metal–organic framework MIL-101 for volatile organic compounds by quartz crystal microbalance, *Environ. Sci. Technol.* 45 (2011) 4490–4496.
 - [29] L. Jia, J. Shi, C. Long, F. Lian, B. Xing, VOCs adsorption on activated carbon with initial water vapor contents: Adsorption mechanism and modified characteristic curves, *Sci. Total Environ.* 731 (2020) 139184.
 - [30] T. Xu, P. Zhang, H. Zhang, Ultrathin 6- MnO_2 nanoribbons for highly efficient removal of a human-related low threshold odorant - acetic acid, *Appl. Catal. B: Environ.* 309 (2022) 121273.
 - [31] L. Miao, J. Wang, P. Zhang, Review on manganese dioxide for catalytic oxidation of airborne formaldehyde, *Appl. Surf. Sci.* 466 (2019) 441–453.
 - [32] H. Zhang, S. Sui, X. Zheng, R. Cao, P. Zhang, One-pot synthesis of atomically dispersed Pt on MnO_2 for efficient catalytic decomposition of toluene at low temperatures, *Appl. Catal. B: Environ.* 257 (2019) 117878.
 - [33] K. Zhou, W. Ma, Z. Zeng, X. Ma, X. Xu, Y. Guo, H. Li, L. Li, Experimental and DFT study on the adsorption of VOCs on activated carbon/metal oxides composites, *Chem. Eng. J.* 372 (2019) 1122–1133.
 - [34] B.C. Trung, L.N.Q. Tu, L.D. Thanh, N. Van Dung, N.T. An, N.Q. Long, Combined adsorption and catalytic oxidation for low-temperature toluene removal using nano-sized noble metal supported on ceria-granular carbon, *J. Environ. Chem. Eng.* 8 (2020) 103546.
 - [35] W.-K. Kim, K. Vikrant, S.A. Younis, K.-H. Kim, P.M. Heynderickx, Metal oxide/activated carbon composites for the reactive adsorption and catalytic oxidation of formaldehyde and toluene in air, *J. Clean. Prod.* 387 (2023) 135925.
 - [36] T. Dong, W. Liu, M. Ma, H. Peng, S. Yang, J. Tao, C. He, L. Wang, P. Wu, T. An, Hierarchical zeolite enveloping Pd-CeO₂ nanowires: an efficient adsorption/catalysis bifunctional catalyst for low temperature propane total degradation, *Chem. Eng. J.* 393 (2020) 124717.
 - [37] Y. Hu, C. Song, C. Li, J. Wang, Two-step pyrolysis of Mn MIL-100 MOF into MnO nanoclusters/carbon and the effect of N-doping, *J. Mater. Chem. A* 10 (2022) 8172–8177.
 - [38] A. Aijaz, A. Karkamkar, Y.J. Choi, N. Tsumori, E. Rönnebro, T. Autrey, H. Shiyama, Q. Xu, Immobilizing highly catalytically active Pt nanoparticles inside the pores of metal–organic framework: a double solvents approach, *J. Am. Chem. Soc.* 134 (2012) 13926–13929.
 - [39] G. Song, G. Shi, L. Chen, X. Wang, J. Sun, L. Yu, X. Xie, Different degradation mechanisms of low-concentration ozone for MIL-100(Fe) and MIL-100(Mn) over wide humidity fluctuation, *Chemosphere* 308 (2022) 136352.
 - [40] B.K. Pandey, A.K. Shahi, R. Gopal, Synthesis, optical properties and growth mechanism of MnO nano structures, *Appl. Surf. Sci.* 283 (2013) 430–437.
 - [41] D. Wang, Y. He, Y. Chen, F. Yang, Z. He, T. Zeng, X. Lu, L. Wang, S. Song, J. Ma, Electron transfer enhancing the Mn(II)/Mn(III) cycle in MnO/CN towards catalytic ozonation of atrazine via a synergistic effect between MnO and CN, *Water Res.* 230 (2023) 119574.
 - [42] J. Gao, Y. Wang, H. Wu, X. Liu, L. Wang, Q. Yu, A. Li, H. Wang, C. Song, Z. Gao, M. Peng, M. Zhang, N. Ma, J. Wang, W. Zhou, G. Wang, Z. Yin, D. Ma, Construction of a sp³/sp² carbon interface in 3D N-doped nanocarbons for the oxygen reduction reaction, *Angew. Chem. Int. Ed.* 58 (2019) 15089–15097.
 - [43] K.C. Kwon, K.S. Choi, S.Y. Kim, Increased Work Function in few-layer graphene sheets via metal chloride doping, *Adv. Funct. Mater.* 22 (2012) 4724–4731.
 - [44] L.-F. Zhai, Y.-Y. Chen, Y. Hu, Y.-X. Pan, M. Sun, J. Yu, Y. Wang, W. Kong, MOF-derived MnO@C with high activity for electric field-assisted catalytic oxidation of aqueous pollutants, *J. Hazard. Mater.* 439 (2022) 129670.
 - [45] H. Lan, J. Zhou, Z. Hou, X. An, H. Liu, J. Qu, Defect modulation of MOF-derived ZnFe₂O₄/CNTs microcages for persulfate activation: enhanced nonradical catalytic oxidation, *Chem. Eng. J.* 431 (2022) 133369.
 - [46] M. Zhang, Q. Dai, H. Zheng, M. Chen, L. Dai, Novel MOF-derived Co@N-C bifunctional catalysts for highly efficient Zn–air batteries and water splitting, *Adv. Mater.* 30 (2018) 1705431.
 - [47] C. Yin, C. Pan, Y. Pan, J. Hu, Hierarchical spheroidal MOF-derived MnO@C as cathode components for high-performance aqueous zinc ion batteries, *J. Colloid Interface Sci.* 642 (2023) 513–522.
 - [48] Y. Huang, Y. Liu, D. Tang, W. Li, J. Li, Freestanding MOF-derived honeycomb-shape porous MnOC@CC as an electrocatalyst for reversible LiOH chemistry in Li-O₂ batteries, *ACS Appl. Mater. Interfaces* 15 (2023) 23115–23123.
 - [49] R. Shokry, H.M. Abd El Salam, D. Aman, S. Mikhail, T. Zaki, W.M.A. El Roubay, A. A. Farghali, W. Al Zoubi, Y.G. Ko, MOF-derived core-shell MnO@Cu/C as high-efficiency catalyst for reduction of nitroarenes, *Chem. Eng. J.* 459 (2023) 141554.
 - [50] F. Lin, Z. Wang, Z. Zhang, L. Xiang, D. Yuan, B. Yan, Z. Wang, G. Chen, Comparative investigation on chlorobenzene oxidation by oxygen and ozone over a MnO_x/Al₂O₃ catalyst in the presence of SO₂, *Environ. Sci. Technol.* 55 (2021) 3341–3351.
 - [51] K. Zhao, L.-X. Zhang, H. Xu, Y.-F. Liu, B. Tang, L.-J. Bie, Single-ion chelation strategy for synthesis of monodisperse Pd nanoparticles anchored in MOF-808 for highly efficient hydrogenation and cascade reactions, *Nanoscale* 14 (2022) 10980–10991.
 - [52] Y. Zhao, H. Zhou, W. Chen, Y. Tong, C. Zhao, Y. Lin, Z. Jiang, Q. Zhang, Z. Xue, W.-C. Cheong, B. Jin, F. Zhou, W. Wang, M. Chen, X. Hong, J. Dong, S. Wei, Y. Li, Y. Wu, Two-step carbothermal welding to access atomically dispersed Pd1 on three-dimensional zirconia nanonet for direct indole synthesis, *J. Am. Chem. Soc.* 141 (2019) 10590–10594.
 - [53] Q. Sun, B.W.J. Chen, N. Wang, Q. He, A. Chang, C.-M. Yang, H. Asakura, T. Tanaka, M.J. Hülsey, C.-H. Wang, J. Yu, N. Yan, Zeolite-encaged Pd–Mn nanocatalysts for CO₂ hydrogenation and formic acid dehydrogenation, *Angew. Chem. Int. Ed.* 59 (2020) 20183–20191.
 - [54] Z. Li, S. Ji, Y. Liu, X. Cao, S. Tian, Y. Chen, Z. Niu, Y. Li, Well-defined materials for heterogeneous catalysis: from nanoparticles to isolated single-atom sites, *Chem. Rev.* 120 (2020) 623–682.
 - [55] X. Zheng, Z. Wu, J. Yang, S. Rehman, R. Cao, P. Zhang, Metal–organic gel derived N-doped granular carbon: remarkable toluene uptake and rapid regeneration, *ACS Appl. Mater. Interfaces* 13 (2021) 17543–17553.
 - [56] C. Wang, H. Yin, P. Tian, X. Sun, X. Pan, K. Chen, W.-J. Chen, Q.-H. Wu, S. Luo, Remarkable adsorption performance of MOF-199 derived porous carbons for benzene vapor, *Environ. Res.* 184 (2020) 109323.
 - [57] X. Zheng, W. He, S. Rehman, P. Zhang, Facile Synthesis of hydrophobic metal–organic gels for volatile organic compound capture, *ACS Appl. Mater. Interfaces* 12 (2020) 41359–41367.
 - [58] Z. Yan, Z. Xu, L. Yue, L. Shi, L. Huang, Hierarchical Ni–Al hydrotalcite supported Pt catalyst for efficient catalytic oxidation of formaldehyde at room temperature, *Chin. J. Catal.* 39 (2018) 1919–1928.
 - [59] M. Guo, K. Li, H. Zhang, X. Min, X. Hu, W. Guo, J. Jia, T. Sun, Enhanced catalytic activity of oxygenated VOC deep oxidation on highly active in-situ generated GdMn₂O₅/GdMnO₃ catalysts, *J. Colloid Interface Sci.* 578 (2020) 229–241.
 - [60] K. Rintamee, K. Föttinger, G. Rupprechter, J. Wittayakun, Ethanol adsorption and oxidation on bimetallic catalysts containing platinum and base metal oxide supported on MCM-41, *Appl. Catal. B: Environ.* 115–116 (2012) 225–235.
 - [61] S. Xu, K.-F. Zhang, Y.-K. Ma, A.-P. Jia, J. Chen, M.-F. Luo, Y. Wang, J.-Q. Lu, Catalytic oxidation of dichloromethane over CrFeO mixed oxides: improved activity and stability by sulfuric acid treatment, *Appl. Catal. A: Gen.* 636 (2022) 118573.
 - [62] J. Saavedra, H.A. Doan, C.J. Pursell, L.C. Grabow, B.D. Chandler, The critical role of water at the gold-titania interface in catalytic CO oxidation, *Science* 345 (2014) 1599–1602.